

On the simulation of up-looking and down-looking high-resolution radiance spectra using two different radiative transfer models

Rolando Rizzi¹, Marco Matricardi and
Ferenc Miskolczi²

Research Department

¹ Dept. of Physics, Università degli Studi, Bologna, Italy

² Current affiliation: Raytheon STX Corporation

September 2001

Accepted for publication in Applied Optics

For additional copies please contact

The Library
ECMWF
Shinfield Park
Reading, Berks RG2 9AX

library@ecmwf.int

Series: ECMWF Technical Memoranda

A full list of ECMWF Publications can be found on our web site under:
<http://www.ecmwf.int/pressroom/publications.html>

© Copyright 2001

European Centre for Medium Range Weather Forecasts
Shinfield Park, Reading, Berkshire RG2 9AX, England

Literary and scientific copyrights belong to ECMWF and are reserved in all countries. This publication is not to be reprinted or translated in whole or in part without the written permission of the Director. Appropriate non-commercial use will normally be granted under the condition that reference is made to ECMWF.

The information within this publication is given in good faith and considered to be true, but ECMWF accepts no liability for error, omission and for loss or damage arising from its use.



Abstract

Measurements of up-looking spectral radiances measured during CAMEX-1 and down-looking ones measured at one of the ARM sites are compared to simulations using two different line-by-line models.

Simulations are performed in tightly controlled conditions to verify the behavior of the models. Spectra computed at higher sampling are used to study the spectral structure of the differences between simulations and measurements.

A revised list of water vapor spectroscopic parameters is used to test the impact of improved spectroscopic data on the accuracy of the line-by-line calculations.

The sensitivity of the results to errors resulting from uncertainties in the input atmospheric temperature and humidity profiles is also investigated.

OCIS codes:

010.1290 Atmospheric Optics

280.0280 Remote Sensing

010.3920 Meteorology

300.6340 Spectroscopy: infrared

1. Introduction

A prerequisite for exploiting satellite radiance data for Numerical Weather prediction (NWP) by use of a variational analysis scheme (for example, 1D-Var described by Eyre et al¹ for a single profile retrieval or 4D-Var described by Rabier et al² for a global NWP analysis) is the ability to simulate radiances from an input atmospheric profile. To achieve this, a radiative transfer (RT) model is used. The computation of the radiances from the NWP model profile and surface parameters is commonly referred to as the “forward model”. The variational approach to assimilation of data into a NWP system involves¹ the definition of the observation-error covariance matrix that is used to specify errors associated with radiance data. The observation-error covariance matrix is the sum of the instrumental-error covariance matrix and the forward-model-error covariance matrix, the latter being based on the estimate of errors associated with RT models. For radiance assimilation in NWP, fast RT models³ are used that are generated from accurate transmittances computed using line-by-line models. In principle fast RT models should not add significantly to the errors generated by uncertainties in the spectroscopic data used by the line-by-line model so that these errors make most of the contribution to the forward-model-error matrix.

The current generation of satellite sounders have limited vertical resolution. The Infrared Atmospheric Sounding Interferometer (IASI)⁴ and the Atmospheric Infrared Sounder (AIRS)⁵ have been designed as pre-operational advanced infrared sounders on the next generation of operational meteorological polar orbiters. The IASI and AIRS systems will provide high spectral resolution allowing improved extraction of temperature, moisture, and some minor constituents. NWP centers are not expected to use the thousands of IASI/AIRS channels. This means that a subset, or appropriate combination, of channels should be defined for assimilation purposes so that the information content present in the whole spectrum is not significantly degraded. RT errors are an important consideration in channel selection. In fact guidance is needed priori to the channel selection as to which procedure to adopt for the retrieval to minimize the effects of system errors, and of forward model errors in particular.

The objective of this paper is to quantify differences due to different forward model mechanics and to the quality of the spectroscopic databases used in the forward model computations and to identify spectral regions where forward model errors are smallest. Two test cases are studied by comparing simulated spectra with spectra measured during the first Convection and Moisture Experiment (CAMEX-1)⁶ campaign and with spectra measured at the Atmospheric Radiation Measurement (ARM) 7 site. Both data sets were prepared and distributed by the Cooperative Institute for Meteorological Satellite Studies (CIMSS).

A special emphasis is given to the up-welling radiance spectra measured by the High-resolution Interferometer Sounder (HIS)⁸ instrument during the CAMEX-1 campaign, because of the similarity in viewing geometry with AIRS and IASI.

The line-by-line codes used to simulate the spectra are described in section 1. Measurements are detailed in section 2 whereas the results for the CAMEX-1 case and the ARM case are discussed in section 3 and 4 respectively. Conclusions are given in section 5.

2. Line-by-line codes

2.1 GENLN2

Line-by-line simulations at ECMWF were performed by use of the GENLN2⁹, a general-purpose line-by-line atmospheric transmittance and radiance model. The line-by-line calculation involves calculating transmittances in several atmospheric layers for each of the gases that are spectroscopically active over the spectral range of interest in wave-number space. The atmosphere is subdivided into a number of layers within which the gas is considered homogeneous and is represented by appropriate Curtis-Godson absorber weighted mean parameters. Mean temperature, pressure and gas amount are defined for each gas along the actual ray trajectory within the layer (gas path) and since within a path the gas is considered homogeneous, the line-by-line computation of the absorption coefficient proceeds for each gas path at each point of the wave-number grid. In principle one could choose a wave-number grid fine enough that the narrowest line is adequately sampled to evaluate the absorption coefficient for every line at every wave-number grid point. Given the excessive amount of computer time and storage required by such approach, the GENLN2 algorithm is based on the assumption that a wider wave-number grid can be reasonably used in the wings of lines whereas a fine grid is required over the line center where the line profile is changing rapidly. In the GENLN2 computations performed at ECMWF the wave-number range is divided into a number of 1 cm^{-1} constant spacing intervals (wide mesh) as shown in Fig.1.

The line-by-line computation then proceeds in two stages. The first stage involves the computation of the absorption due to the wings of lines whose centers fall within the range 1 cm^{-1} to 25 cm^{-1} from the wide mesh boundaries. For these lines, absorption is computed at the lower boundary, center, and upper boundary of the wide mesh interval. For the lines whose centers are further than 25 cm^{-1} from the wide mesh boundary, the absorption contribution of the line wing is included by means of a continuum for H_2O and CO_2 as explained below. Once the contributions from all far-off lines wings have been considered, a quadratic interpolation between the three values at the wide mesh points gives the total line wing absorption at intermediate points. The second stage of the computation involves the absorption calculation over a fine grid obtained by dividing the wide mesh interval into 1000 points. All the lines whose centers lie within 1 cm^{-1} of the wide mesh boundaries are included. The



interpolated absorption due to the wings of the lines further than 1 cm^{-1} from the wide mesh boundary are then added to the fine-pass absorption to give the total line absorption at each fine grid point within the wide mesh.

Therefore, there is no spectral integration involved in the GENLN2 calculation of quantities in the fine mesh. These will be truly monochromatic values on the fine mesh of either a spectral function such as the absorption coefficient or a spectral density (by wave number) proportional to a distribution function such as the spectral intensity of a line e.g. the Lorentzian. GENLN2 calculations were not performed for very weak lines. The minimum line strength is determined by considering an Elsasser distribution of lines to represent the extreme case of a tight absorption band of low optical depth. The lines have half width 0.1 cm^{-1} , peak separation 0.01 cm^{-1} and constant strength S . For a given path j the lines are considered not to be significant if the transmission of such a line distribution is greater than 0.99999. This means that for a line to be used, $S_j u_j$ (u_j is the gas path amount) must be greater than a minimum value. In the wide mesh calculations we rejected lines for which $S_j u_j < 10^{-7}$ and in the fine mesh calculations we rejected lines for which $S_j u_j < 10^{-8}$. The accuracy of the line-by-line computations should not be affected by the rejection of very weak lines. For this paper we found that the inclusion of all the lines in the GENLN2 computations had no significant impact on the computed spectra (when compared with the baseline spectra differences were never greater than 0.001 K) whereas the computational time was reduced six-fold. Note that the condition used for $S_j u_j$ is relevant for lower and middle atmosphere studies only, for other applications different values should be used. Heavy molecules were modeled by using high-resolution cross-sectional data. The line strengths and half-widths are adjusted to the path pressure and temperature and Doppler broadening of the spectral lines is taken into account. The Voigt¹⁰ line shape was adopted for most cases to describe the effects of both pressure and Doppler line broadening. For some gases the Voigt line shape is not adequate and effects such as line mixing and non-Lorentzian line wing effects must be considered. In GENLN2 there is a CO₂ line shape option that includes the effects of line mixing and sub-Lorentzian line wings. If data is available, CO₂ Q-branch line mixing can be included out to an arbitrary 10 cm^{-1} from line center. At greater distances from line center, a sub-Lorentzian line shape is used¹¹. If no line-mixing data is available then the sub-Lorentzian line shape is used everywhere. CO₂ line mixing was fully accounted for in the computations by using line mixing coefficients from Strow et. al.¹². Note that since the line mixing coefficients depend on the line strengths and widths, they must be used in conjunction with the lines for which mixing coefficients have been calculated. The water vapor continuum is computed using the semi-empirical approach of Clough et al.^{13,14} (CKD version 2.1) and in addition to H₂O, a CO₂ continuum type absorption is also included. The CO₂ continuum is computed using the GENLN2 line shape and is stored in the code at temperatures of 230K, 250K and 296K. For a given wave number, the continuum at a particular path temperature is obtained by interpolation between these values. Finally the pressure-broadened band of N₂ at 2350 cm^{-1} (Ref. 15) and that of O₂ at 1550 cm^{-1} (Ref. 16 and 17) are also included as broadband continuum contributions to the absorption.

2.2 HARTCODE

The high-resolution atmospheric radiative transfer code (HARTCODE) was developed under the support of the International Centre for Theoretical Physics, Trieste, Italy^{18,19}. The basic motivation for the code development was to keep the numerical accuracy of the spectral atmospheric transmittance and radiance computations under strict control. At that time the code was a purely a research tool to identify and estimate the code mechanics related factors affecting code accuracy. The code went through several upgrades and improvements, but still its basic feature was kept intact. Namely, the ultimate numerical accuracy can be controlled, and in case of need, the code is able to fall back to its clumsy but otherwise mathematically rigorous version of extreme numerical accuracy.



During the development of the code, most of the efforts were concentrated on the accurate re-layering and wave number integration procedures. Since the recent comparison was conducted with fixed layers and nadir viewing, we shall not go into the details of the layering and handling the trajectory in a spherical refractive geometry.

In the HARTCODE the wave number domain is divided into steps. The computation passes through the wave-number domain from a starting wave number to an ending wave number in these steps. The length of a step is optional, and usually limited by the computer's capability. Typically, steps can have values of 0.5, 1.0 and 2 cm^{-1} and output blocks of the required spectral quantity will be generated at each step.

The steps are further divided into smaller sub-intervals, (SI), which represent the resolution of the code (see Fig. 1 (b)). The output blocks of each step will contain the integrated (or averaged) spectral optical depth, transmittance and radiance over each SI. The length of a sub-interval is limited only by a parameter statement of the code, and typical length settings for 1 cm^{-1} steps normally range from 0.001 to 1.0 cm^{-1} .

Depending on the positions of all the lines falling within SI, a fine mesh structure is created. In this fine mesh structure, each line center is represented with one point, and starting from each line center several additional points are added. The positions of the additional points are depending on the minimal Voigt half-width along the whole trajectory, and on an input scaling factor. The scaling factor controls the number of mesh points to be added within one half-width from the line center. Getting farther from the line center this number will decrease according to a power function. The above mesh structure defines the sub-sub-intervals (SSI) over which Gaussian quadrature is applied to perform the wave number integration. The accuracy of the wave number integration over SI will depend on the number of SSI and the (user-defined) order of Gaussian quadrature used in each SSI. In the present computations 4 SSI intervals for the first half width distance from the center were used and a 3-point Gaussian quadrature in each SSI interval.

Two input parameters control the line contribution to a given monochromatic Gaussian mesh point. These two input scaling factors are given in multiples of the maximum Voigt half-width (MVH), of a given layer, and as such, they are depending on the pressure. Using 10 and 100 for these input parameters, at around 1000 hPa pressure, and assuming 0.1 cm^{-1} MVH, the joining wave-number regions are marked by the distances of 1 and 10 cm^{-1} from both end points of the step.

The lines between the end-points of a step and the beginning of the two side intervals are treated similarly to the lines within the step. They are always contributing to the monochromatic optical depth using the proper Voigt line shape. However, there is a further option to treat the lines that are marked as very weak lines. A third input parameter can be set to define the distance from the center of a weak line where the line contribution will be cut off.

The line contribution from the regions between the two marking distances may be computed (optionally) by a simplified way. At high pressure it uses Chebyshev polynomials of fourth order, while at low pressure we use linear interpolation over a non-uniform mesh structure specially generated for this purpose. The use of this option to compute the side contributions may significantly reduce the accuracy of the optical depths, or transmittances, but has less serious effects on the radiances.



In the recent version of HARTCODE the contribution from the lines being further than the extent of the outer side-intervals are not considered. This contribution is generally referred as far-wing absorption. Accurate far-wing absorption can only be computed from accurate line shape functions. Far from the line centers the shapes of the absorption lines are, however, not sufficiently well known, and significant error may be introduced into the related absorption term. Whenever experimental results prove with sufficient accuracy that a particular molecule has continuum type absorption, then the best strategy is to consider this absorption by a parameterized wave-number dependent database. The water vapor continuum is the CKD version 2.4^{12,13}. The treatment of N₂ and O₂ continua is the same as in GENLN2.

HARTCODE computes the CO₂ Q band line-mixing either with first order line mixing or with the detailed computation of the matrix element of the relaxation operator 20. The second option was used for the present computations.

3. Measurements

3.1 CAMEX-1

The data used for this case study belongs to the first Convection and Moisture Experiment CAMEX-1 field campaign and consists of the up-welling radiance spectrum measured by the HIS⁸ during the third northbound pass of the ER-2 aircraft along the Virginia/Maryland coast on 29 Sept 1993, from an altitude of approximately 20 km. The distribution files contain the mean and an estimate of uncertainty around the mean for each wave-number sample of the calibrated radiance obtained during the period 03:47:40 UT to 03:54:59 UT. Details of the methodology used to process the HIS data and the in-situ observations were also provided. Some of the information is reported here for convenience.

The HIS data is nadir viewing with a sample time of 6 seconds, without motion compensation, yielding a 2x3 km footprint for every 6 second sample. The spectrum is recorded simultaneously as three independent bands, and is provided as unapodised radiances with the finite field-of-view effect removed. Only data within the optical filter band-pass is included in the data set. Each calibration cycle contains 12 earth views, 4 hot blackbody views, and 4 cold blackbody views in a repeating sequence. The 12 earth views overlap along the flight track to give a continuous strip 2km wide and 12km long. The data provided contain an average of data from four consecutive calibration cycles. This sample average views a strip of ocean about 2km wide and 48 km long. The actual linear distance along the flight track is more than 48 km since no earth data is collected during views of the calibration blackbodies at the end of each calibration cycle. Basic information on HIS quantities referred to in the text are provided in Table 1.

Table 1 – HIS Parameters

Band	Band 1		Band 2		Band 3	
Free Spectral Range (cm ⁻¹)	564.2500	1128.5000	987.4375	1974.8750	1974.8750	2962.3125
Optical Filter Range (cm ⁻¹)	600	1080	1080	1800	2050	2600
Spectral Spacing (cm ⁻¹)	.2755127		.4821472		.4821472	
Maximum Delay (cm)	1.550731		.683588		.518514	
Unapodised Resolution (cm ⁻¹)	0.322429		.731435		.964294	



The estimate of the uncertainty of the averaged radiances is computed as the standard deviation of the 48 earth views around their mean divided by the square root of the number of samples. The standard deviation is spectrally highly variable and is likely to contain both signal variability due to random instrument noise and that caused by the changing atmospheric conditions during the flight. As there is no independent information on instrument noise, it is not possible to separate the various contributions. There are large spectral regions where the S/N is particularly low since the averaged signal is low or the atmospheric signal variability is large and this is valuable information to interpret correctly the differences with the simulated data. In all figures the standard deviation derived from the measurement set is indicated by the symbol std.

The in-situ data, called the CAMEX Validation Atmosphere for 29 Sept 1993 04:00 UT, contains altitude, pressure, temperature, relative humidity and ozone concentration from 1003 hPa to 5 hPa, obtained from blending of measurements from different radiosondes. A special surface level at 1018 hPa is included, designed to represent the ocean environment consistent with the HIS aircraft data. The sea surface (skin) temperature was set to 293K which is close to the temperature at the peak of the inversion layer in the Wallops 4:00 UT radiosonde observation and to the temperature obtained by comparing line-by-line FASCODE²¹ simulations with HIS data²². There are no direct measurements of the near surface air temperature offshore. The dataset contains also estimates of extreme relative humidity values, obtained primarily from comparing the sonde profile to the lidar profiles⁶.

3.2 The ARM case

The data used for this study belongs to the Department of Energy (DOE) Atmospheric Radiation Measurement (ARM) Program 7 and were measured at the Cloud and Radiation Testbed (CART) Southern Great Plains (SGP) Central Facility. The case belongs to a Water Vapor Intensive Observing Period (WVIOP) and contains the averaged radiances from two coincident observations of the down-welling atmospheric infrared spectra at the surface for a zenith view from 05 to 07 UT of 26 September 1997. The number of spectra in the averaging period was 15 for both instruments. The radiation measurements were complemented with best estimate atmospheric temperature and water vapor profiles.

The radiometric observations were made with two interferometers, called Atmospheric Emitted Radiance Interferometer 23 - AERI-00 and AERI-01. AERI-01 was the CART operational instrument while AERI-00 was a prototype. The data used in the exercise are the unapodised values at a spectral resolution of approximately 0.48 cm⁻¹, corresponding to a maximum optical delay of about 1.037 cm. A finite-field-of-view correction was applied to remove the effect of instrument self-apodisation. The data from both instruments was complemented with uncertainty estimates determined from the standard deviation of the spectra over the averaging period. The latter includes also true atmospheric variability during the averaging period, but the time period from 05 to 07 UT was chosen because it was a relatively stationary situation, characterized by clear sky and relatively low water vapor level. The comparison of the measurements from the two instruments showed excellent agreement with water vapor amounts down by a factor of three with respect to earlier comparisons 24.

The best estimate profiles are the results of an effort by the data provider to merge information from different water vapor measurement techniques from instruments assembled at the SGP CART site 22. These included sondes, tower sensors, microwave radiometers, raman lidars, solar observations and others. The profiles are complemented with error profiles. More information can be obtained from the ARM web site 24.



4. Results for CAMEX-1 case

4.1 Results from HARTCODE and GENLN2

Several simulated data sets were prepared using the LBL codes described in section 1. Each set served a different objective. The most important objectives of the exercise were to shed light in the differences produced by different code “mechanics” when applied to the same atmospheric profile and to identify spectral regions where forward model errors are smallest. A protocol was agreed to define the so-called Test Case (TC).

The up welling radiances at flight altitude were computed in very controlled conditions:

- a predefined atmospheric layering defined by corresponding pressure and altitude levels; temperature, and level concentrations for 14 selected gaseous species (H_2O , CO_2 , O_3 , N_2O , CO , CH_4 , O_2 , NO , SO_2 , NO_2 , N_2 , CCl_3F , CCl_2F_2 and CCl_4);
- mean pressure, altitude and temperature, and layer integrated gas amount for each atmospheric layer provided as a check for consistency among the processing done by the two codes;
- a given skin temperature (293 K) and surface emissivity (sea) set to unity.

All remaining input and internal parameters were not prescribed. The sampling and resolution of the high spectral resolution (HR) computations were code dependent, based on the intrinsically different methodologies and definitions adopted by the two codes to compute the spectra, as it was discussed in section 1. The spacing of the monochromatic GENLN2 radiance computations is 0.001 cm^{-1} while HARTCODE produces radiances integrated within 0.005 cm^{-1} intervals with a spacing of 0.005 cm^{-1} . Uniformity was not sought for water vapor, oxygen and nitrogen continuum absorption coefficients, or for the spectroscopic databases to be used. The GEISA-97²⁵ database was adopted for the HARTCODE computations, while HITRAN-96²⁶ (supplemented with a compilation of lines from the HITRAN-92²⁷ database for the CO_2 line mixing calculation) was used with GENLN2.

Of course the simulations performed for the Test Case, and whose results are presented in this section, are not intended as best possible when compared to the measured data. Other simulations were performed to exploit the capabilities of the two LBL codes. Some of the results from the latter are also presented and discussed in this paper which is however focused onto the primary objectives.

The methodology used to simulate the HIS measurements, in each of the three bands, involve the following steps:

1. HR spectra are computed for the spectral range from 500 to 3500 cm^{-1} , much larger than the total interval covered by the free spectral range of the 3 HIS bands;
2. the HR spectra are interpolated to an interval which is a power-of-2 sub-multiple of the HIS spectral spacing ds (given in Table 1);
3. the interpolated spectrum is tapered smoothly to zero outside the optical filter range;
4. the interferogram containing the same information as the interpolated HR spectra is computed by FFT techniques;



5. the interferogram is truncated beyond the maximum delay given for each band and zero filled to the number of intervals of the final convoluted spectrum;
6. the truncated and zero-filled interferogram is inverse Fourier transformed to produce the simulated spectra that can be compared directly with the HIS data.

The above processing was performed on both HR radiance sets using exactly the same code. The resulting sets are referred to in the figures as GE for the set produced using GENLIN2 and HA for HARTCODE.

To understand the performance of the two codes the average (bias) and root-mean-square-error (rms) of the difference between the simulated and measured radiance are computed over intervals of width 50 cm^{-1} (except at the extremes of bands where it may be larger: for example, the last interval for band 1 is 1000-1080). Finally the relative bias and rms values are computed by dividing the bias and rms values by the average radiance in each spectral interval.

These relative values are plotted, as percentile values, in Fig. 3, for HIS band 1 and 2. The results in band 1 indicate that the two LBL codes produce very similar results. The peak in the rms curves around 740 cm^{-1} shows that there are problems in simulating the high frequency branch of CO_2 15-micron band. The bias for both codes is generally positive and lower than 1% except in the range $950\text{-}1040 \text{ cm}^{-1}$, where the increase in bias reflects a poor performance in simulating the ozone band, possibly caused by an inadequate representation of the ozone vertical distribution or by the relatively coarse atmospheric layering in the upper part of the profile. Beyond 1040 cm^{-1} the increase in relative bias is most likely to be linked with the rapid increase of measurement error, defined by the standard deviation discussed previously and shown in Fig.3 with the dotted line. The rms error is generally below 2% except beyond 1050 cm^{-1} for the same reason noted above, and is slightly lower than the measurement standard deviation (std) from 820 to 980 cm^{-1} .

In band 2, although the overall performance of the codes is very similar, slightly better results are obtained by each code in different spectral ranges across the water vapor band. A local rms maximum is seen around 1320 cm^{-1} , a spectral region where a large number of water vapor and methane lines are present. The sharp increase in rms above 1500 cm^{-1} occurs in a region where std is sharply increasing.

The results for band 3 (Fig. 4) indicate that both bias and rms are larger than in the other two bands and that bias is the major error term. One notes that between 2250 to 2340 cm^{-1} a region of high scatter is observed in correspondence with large values of std. The largest (negative) bias, about 40%, is found around 2330 cm^{-1} .

It is sometimes convenient to express the radiance differences in terms of noise-equivalent- delta-temperature (NEDT) at some reference blackbody temperature, as NEDT is often used to specify the noise performance of satellite-borne sounding sensors. Therefore the estimated HIS measurement error and the rms error of the simulated versus measured radiances, over same 50 cm^{-1} intervals as previously described, are shown in Fig. 5, expressed as NEDT for a blackbody temperature of 280K. There is no need however of further discussion as the NEDT figures convey the same information as displayed in the preceding figures. In band 1 values range from 0.25 to 1.5 K, while in band 2 the NEDT ranges from 0.25 to 0.6 K. The NEDT values for band 3 are not shown since measurement NEDT is quite large and only in the interval 2060 to 2240 cm^{-1} the measurement error (std) is



sufficiently low to allow proper evaluation of the behavior of the two codes. In the latter range NEDT values are fairly constant around a mean value of 0.63 for GENLN2 and 0.65 for HARTCODE.

A number of important issues are highlighted by Fig 3 to 5, besides the differences in the results by the two codes. Firstly there are spectral ranges (from 700 to 800 cm^{-1} , and from 1200 to 1500 cm^{-1}) where the discrepancy with the measurements is much higher than std, and therefore there is a need for improvement in the computations. HARTCODE for example has too large an NEDT around 1600 cm^{-1} , close to the center of the water vapor vibrational band, when compared to GENLN2, although both code relative rms is smaller than std.

Secondly the magnitude of the differences between simulations and measurements is, in many spectral regions, much larger than the difference between the two codes, which indicates that the problems encountered, for example in simulating the high frequency side of the CO_2 band, are likely of spectroscopic nature. Some scope for improvement is however possible in band 2 as the bias between the codes is larger, especially close to the water vapor vibrational resonant frequency.

A third aspect is that the differences (with the measurements) of the two codes are extremely correlated. The cross-correlation at lag zero is 0.99998, 0.99997 and 0.99969 for band 1 to 3 respectively. At larger lag the correlation falls below 0.4 in all bands. An example of such very high correlation can be seen in Figures 6(a) to 6(d). The lower dotted curve is the HIS radiance spectrum (the curve is shown only to understand where the absorption "lines" are located and its ordinate scale is irrelevant), the upper solid (dotted) is HA (GE) minus HIS radiance and the two dashed curves identify the positive and negative HIS estimated measurement error as specified in section 2.1. The spectral intervals are chosen for their importance in the atmospheric temperature and humidity nadir-sounding problem and because the measurement error is lower than the difference between simulation and measurement. The x-axis position of the vertical lines from the bottom in the three figures is the central frequency of the strongest absorption lines used in the simulations and their vertical extent is a measure of their strength (the scale is irrelevant). Fig. 6(a) shows that both codes underestimate the measurement in proximity of the center of the CO_2 lines while overestimate in the weak absorbing regions between the lines. The distribution of strongest absorption in these intervals also shows very clearly that the main absorption features are sometimes due to single lines, as in Fig. 6(a), but most of the time are the result of complex interaction between many lines and gaseous species. For example the negative differences around 791.6 cm^{-1} in Fig. 6(b) are due to several closely spaced CO_2 lines of the Q-branch, a single strong (water vapor) line is responsible for the complex error structure at 784.5, 793.8 and 795.8, but three strong lines are responsible for the feature around 799 cm^{-1} . It is well known that the situation is most complicated in regions where water vapor is the major absorber, as in the range from 1400 to 1450 cm^{-1} shown in Fig. 6(c). Here complex absorption is taking place from a multitude of intense water vapor lines.

A discussion on the results for band 3 is made more difficult because of the magnitude of experimental errors which is smaller than the difference with measurements only in a small interval from 2080-2200 cm^{-1} , which is shown in Fig 6(d). The quantities plotted in this case is measured brightness temperature (lower dotted curve) and difference in BT. The strongest discrepancies (at 2090, 2115, 2136, 2161 cm^{-1}) are due to interaction of several intense water vapor lines. The presence of CO absorption produces an alternating error structure with the negative maxima in phase with CO line centers, whose amplitude is comparable to the measurement error. No correlation is apparent between the differences and the highly regular N_2O line structure that is not resolved by the measurements, nor with the very complex but weaker line structure of ozone. Due to the high correlation between

the simulations, one can infer that some of the “measurement noise” is in fact due to actual atmospheric variability.

The noted high correlation between the results of the two codes in band 1 and portions of band 2 and 3 is an important feature since it demonstrates that, in those ranges, most of the discrepancies with measurements are not due to the way a particular LBL code performs the integration of the line contribution (its mechanics), but to the insufficient knowledge in basic spectroscopy, for example the shape of an isolated line and of mixed lines, the quality of the line parameters contained in the databases and lines that are not yet documented in the same. This is particularly true for the ranges where the simulations by both codes are most similar. Further evidence for this conclusion is the way the comparison is performed, starting from exactly the same atmospheric layering structure.

When the emission spectrum is sampled at high resolution, as by next generation sounders IASI and AIRS, the question arises whether it is more appropriate to utilize only, or preferably, the measurements taken in the weakly absorbing regions between the lines, the argument being that these regions are less sensitive to changes in the spectral calibration of the instrument and produce theoretically more vertically resolved weighting functions. The examples just given, and many more that are found in different spectral regions, tend to indicate that only in very limited spectral regions the line structure is so regular that we can actually speak of line wing absorption, while in most cases, the situation is more complex.

From the examples given, it appears that an investigation on the spectral structure of the differences between simulation and measurement is still difficult with a spectral spacing like the one adopted so far. Spectra with higher sampling can be used to understand if there is any phase relation between line centers and difference maxima and minima. They were obtained, only for the HARTCODE results, from the same interferograms used previously, both measured and simulated, but padded with trailing zeroes so that the spacing between spectral points is reduced eight-fold. Some of the results are shown in Fig. 7(a) and Fig 7(b). The upper solid curve is the difference between simulations and measurements (at higher sampling), while the lower dashed curve is the “measurement” (at higher sampling). The vertical lines from the bottom of the figures have the same meaning as in previous figures.

The results can be summarized as follows:

- In the important temperature sounding region $730\text{-}770\text{ cm}^{-1}$ (Fig. 7a) the CO_2 line structure has a fairly regular spacing and the largest (negative) deviations are very close, but not coincident with line centers; between the main lines however systematically positive deviations are observed with a magnitude about half the maximum (negative) local “errors”; in presence of isolated water vapor lines these positive deviations are of larger magnitude.
- In the window region (Fig. 7b) the deviations are largest in presence of single or a small group of water vapor lines; the common pattern is a shift from a negative to a positive peak across the line, with the largest difference not coincident with line centers (even in the case of single lines) but shifted by about one half of a HPHW to the high frequency side. In fact, the difference at the line centers (or the center of the strongest line of the group) is usually very small. This behavior is similar to the amplitude difference between two sinc cardinal functions of same width but shifted in central wave number and are an indication that the error



structure can be improved by a slight change of the nominal wavelength of the laser source that is used to simulate the interferograms sampling.

- It was already observed that one cannot speak of wings between lines in the water vapor band and in the region from 2080 to 2200 cm^{-1} . In fact the largest (positive) differences are seen in correspondence with groups of tightly spaced lines and these spectral regions must therefore be treated with increased care.

4.2 Results with extended HITRAN database

During the course of this study a revised list of water parameters^{28,29,30,31,32,33} became available that could be used to test the impact of improved spectroscopic data on the accuracy of the line-by-line calculations. An extension to the GEISA-97 and HITRAN-96 databases was prepared³⁴ that includes the updated water parameters. The extended HITRAN-96 was used to compute a GENLN2 spectrum that was then compared with the one obtained by using the baseline HITRAN-96. A check was made for duplicate lines by comparing the quantum numbers of the line transitions: if a duplicate line was found, the one from the new database was used. The impact of the updated spectroscopic data is shown in Fig. 8 where the relative bias and the relative rms (as defined in section 3.1) are plotted for the HITRAN-96 and extended HITRAN-96 cases. Only regions where significant differences occur are shown. In band-1, the inclusion of new spectroscopic data results in an improvement of the bias figure between 750 and 850 cm^{-1} with a peak value of 0.5% attained at 770 cm^{-1} . A slight improvement in bias is also observed between 650 and 750 cm^{-1} . The rms is slightly reduced throughout the band with most of the reduction being achieved in the 650 to 950 cm^{-1} range. In the water vapor sounding band, band-2, results show that the bias is significantly reduced between 1300 and 1400 cm^{-1} . In particular, at 1325 cm^{-1} , the bias is 0.8% lower than the baseline case. In the other band 2 spectral regions, the bias figure is worsened between 1100 to 1300 cm^{-1} , the bias at 1270 cm^{-1} being 0.6% worse than the baseline case. As for the rms, it is reduced between 1250 and 1520 cm^{-1} and worsened between 1520 and 1700 cm^{-1} where the rms is on average 0.1% higher than the baseline case.

4.3 Sensitivity to change in surface emissivity

In the previous section we have given details of the results for the CAMEX-1 case taking the sea surface emissivity equal to 1. The choice of the skin temperature value was based on simulations performed at CIMSS²² that showed a good match could be obtained between simulated and observed radiances when a value of 293 K was taken with emissivity equal to 1. This choice of the surface parameters does not envisage that the surface emissivity is wave number dependent and can differ appreciably from 1 (it should also be noted that the selection of the surface parameters is dependent on many details of the software used to perform the simulations). Therefore, residual errors are expected to be generated, the effects of non-unit surface emissivity being greater in the case of window channels. These errors cannot be attributed to the line-by-line model itself, but must rather be considered as the result of a less than optimal application of the radiative transfer equation. We expect both forward models to be affected in a similar way so that conclusions drawn on differences produced by different code mechanics are not to be altered. However, if we want to assess the accuracy of the forward model calculations in absolute terms, we need to address the issue of a proper treatment of the surface parameters. Possible errors introduced by assuming unit emissivity were studied by obtaining a GENLN2 spectrum including a variable surface emissivity with the skin temperature test value. A non-unity emissivity means that the reflected downward flux must be explicitly accounted for in the radiative transfer equation. The reflected thermal radiance was computed assuming specular reflection, the case for a flat-water surface. The calculation of the sea surface

emissivity was performed adopting the model of Masuda *et al.*³⁵. The refractive index of pure water based on Hale and Querry³⁶ was adjusted (Friedman³⁷) to the seawater value and then interpolated to each fine grid point to be given as an input with surface wind speed and the zenith angle to compute the rough sea surface emissivity. Since there are no direct measurements of the surface wind speed offshore, we assumed a reference value of 7 m s^{-1} . The choice of this parameter is not critical in that for a nadir view the dependence of the surface emissivity on the wind speed is only marginal. Results are shown in Fig. 9 where the relative bias and the relative rms (computed as usual over intervals of width 50 cm^{-1}) are plotted for the test case and for the spectrum computed with variable emissivity. Because of the net decrease of radiation emitted by the surface, the bias has turned negative in the regions where the effects of a non-unit emissivity are greater. A noticeable feature is the significant reduction of the gradient in the bias curve between 750 and 900 cm^{-1} (this is also a region where the emissivity curve has a steep gradient). The rms is slightly better between 720 and 820 cm^{-1} and significantly better between 1170 and 1230 cm^{-1} . Between 820 and 980 cm^{-1} the rms is significantly worse than the test case. The results shown in Fig. 9 suggest that to get a better agreement with the observations, the skin temperature used in the variable emissivity GENLN2 simulation should be adjusted to a different value. We have incremented the skin temperature by an amount equal to the (absolute) average value of the difference between computed (with variable emissivity) and measured brightness temperatures in the 750 to 1000 cm^{-1} range. We then used the new value to generate a further GENLN2 spectrum that features a variable emissivity and revised skin temperature (293.3 K). The bias is now significantly reduced between 750 and 900 cm^{-1} and between 1100 and 1250 cm^{-1} with the rms figure improved throughout the range. Note however that between 900 and 980 cm^{-1} the bias is slightly worse than the test case value.

The overall effect of having revised the surface parameters has been to significantly improve the absolute accuracy of the line-by-line computations in the window region.

4.4 Sensitivity to changes in humidity profile

As already mentioned in section 2.1, the CAMEX-1 dataset contains estimates of extreme relative humidity values. The modeling of atmospheric radiative transfer is affected by uncertainties in the characterization of water vapor and temperature atmospheric profiles. Although a detailed assessment of the errors resulting from these uncertainties is outside the scope of this paper, the GENLN2 was used to investigate the sensitivity of the HIS radiances to changes in the humidity profile. Errors assumed here are an upper limit and, as shown in Fig. 10, they vary with level, ranging from less than 5% in the lower troposphere to up 200% in the upper troposphere/stratosphere.

For the perturbed case the bias and rms were computed as the difference between the simulated radiance calculated by increasing and decreasing the reference profile by the error profile and the simulated radiance calculated using the reference profile. The relative bias and relative rms were then computed by dividing the bias and the rms by the average measured radiance in the given interval. Figures 11(a) and 11(b) show the relative bias and the relative rms for the reference case whereas for the perturbed case only the relative bias is shown since, as explained below, the bias and rms are comparable. Results are only shown for band-1 and band-2 since for band-3 the measurement error is too large. Band-2 is where the impact of the perturbed profile is greatest. For this band perturbing the humidity profile gives a signal that is well above the discrepancy generated by the forward model at least in the spectral regions where the peak of the weighting functions is attained in the upper troposphere. Elsewhere the signal is comparable with that generated by the forward model. In the temperature-sounding band,



band-1, results are mixed in that the rms is well below the reference level and the bias is at the reference level in most of the spectral range. These results are not straightforward to interpret. It is likely that the relative humidity errors are overestimated in that their inclusion in the forward calculation is expected to generate a signal that is not actually seen. It is worth noting however that since the rms and bias of the signal generated by the error profile are comparable, one effect of perturbing the humidity profile is to impart an offset to the radiance.

5. Results for ARM-WVIOP case

5.1 Results with HARTCODE and GENLN2

We have used for the comparison the measurement by AERI-00, since differences with AERI-01 are very small and in any case much smaller than the standard deviation during the period of integration.

Some characteristics of AERI are given in Table 2. The S/N curve (not shown) is largely variable across the spectrum, generally decreasing with increasing wave number and with relative minima across window regions since the signal measured in window regions when looking at the zenith is relatively low. Our analysis will concentrate below 2200 cm^{-1} since the S/N values at larger wave numbers is below 100. The processing from HR spectra to the final simulated spectra is same as described in section 3.1, account taken of the different properties of AERI.

Table 2 – AERI Parameters

Band	Band 1		Band 2	
	0.	7988.5	0.	7988.5
Free Spectral Range (cm^{-1})	0.	7988.5	0.	7988.5
Optical filter Range (cm^{-1})	520	1800	1800	3020
Spectral Spacing (cm^{-1})	.4821472		.4821472	
Maximum Delay (cm)	1.037028		1.037028	
Unapodised Resolution (cm^{-1})	.4821472		.4821472	

Fig.12 shows the relative bias and rms between simulated and measured radiances, computed over intervals of width 50 cm^{-1} with the same procedure adopted for the CAMEX-1 case. The dotted curve is the AERI relative standard deviation computed over the 50 cm^{-1} intervals. The behavior of the rms and bias curves, for both LBL codes, indicate that a large fraction of the rms values is due to systematic errors and that the AERI-00 estimated averaged noise is much smaller than the discrepancies of the simulations with the measurements. Both simulations underestimate the measured radiances almost in the whole range, and although the spectral behaviour of rms differences is very similar, HARTCODE is colder than GENLN2, especially in the range from 1900 to 2150 cm^{-1} . The cross-correlation at lag 0 between the spectral differences of the two codes is 0.998, and falls below 0.1 from lag 2 on, that is the relative deviations of the two codes are extremely correlated. The differences between the two codes are larger than seen in the CAMEX-1 case.

In the interval between 600 to 1400 cm^{-1} , the largest discrepancies with measurement are found in the most transparent regions. Around 780 cm^{-1} the negative bias peak is in a region of tightly packed H_2O lines, just outside of the CO_2 band. We have noticed discrepancies in this spectral interval also in the CAMEX-1 case. A local minimum in rms is seen from 1250 to 1400 cm^{-1} where important absorption by N_2O and CH_4 occurs on top of H_2O absorption.

The rms curves attain another maximum in the water vapor band (an average value of about 10%) mostly caused again by a systematic underestimation by both codes. A minimum in both bias and rms curves is obtained around 1840 cm^{-1} , where absorption by H_2O is still quite important and then larger bias and rms differences beyond 1900 cm^{-1} are seen in a region of weaker H_2O absorption.

All these results point to the great need to improve our knowledge in basic spectroscopy of the water vapor molecule.

Also the differences between the two codes are a clear indication of the essential role played by water vapor continuum absorption. Two are the main causes for the observed inter-code differences: the use of different continuum coefficients (CKD 2.1 and CKD 2.4), and the fact that the GENLN2 line integration is consistent with the methodology proposed in 13,14, where the contribution of each line beyond 25 cm^{-1} from the line center is attributed to the continuum. Instead the line contribution in HARTCODE is extended to some multiple (in the present computations 100) of the half-width, as discussed in section 1.2. There has been no attempt to optimize the width of the line contribution interval to reduce the negative bias as it would impact also the CAMEX-1 computations.

Self Broadening (SB) CKD-2.1 coefficients are identical to CKD-2.4 in the whole spectral interval of interest. Foreign broadening (FB) coefficients in CKD-2.1 are smaller than CKD.2.4 from 600 to about 800 cm^{-1} and significantly larger between 1860 to 2160 cm^{-1} , as shown in Fig. 13. FB is the dominant source of continuum absorption within the water vapor absorption band. Considering the range of interest in the present work, FB is particularly important between 1350 and 2100 cm^{-1} .

HARTCODE was used to perform some computations also with CKD 2.1 coefficients. It was found that despite the presence of a temperature inversion in the layers close to the ground, an increase in continuum optical depth implies an increase of down-welling radiance at the ground in the transparent regions. From Fig. 12 it is seen that the use of the 2.1 coefficients significantly reduces bias and rms from 1900 to 2150 cm^{-1} , the difference with GENLN2 becoming analogous to what seen between 1080 and 1230 cm^{-1} .

Comparison with the CAMEX-1 results is made difficult by the different measurement geometries that imply, for example, largest radiances in the window regions for down looking measurements and lowest radiance values for up looking measurements. Upon converting the rms figures to NEDT at same reference temperature as for the CAMEX-1 case, we observe in Fig. 14 that these are generally higher than in the CAMEX-1 case. In particular they are more than twice in the range 600 to 1000 cm^{-1} and 1200 to 1400 cm^{-1} and about tenfold higher in the water vapor band. Comparison in the range 1000 to 1200 cm^{-1} and above 1800 cm^{-1} is made difficult by the high noise figure of the HIS instrument.

5.2 Results with extended HITRAN database

The impact of the updated spectroscopic data described in section 3.2 was studied also for the ARM-WVIOP case by comparing the GENLN2 spectrum computed using the extended HITRAN-96 database with the one computed by using the baseline HITRAN-96. Results are shown in figure 15 where the relative bias and the relative rms are plotted for the HITRAN-96 and extended HITRAN-96 cases. Significant differences occur in the 600 cm^{-1} to 1400 cm^{-1} wave number range. The rms values for the extended HITRAN-96 case are always below the values for the baseline case. In particular, a very significant reduction is achieved in the 700 cm^{-1} to 1200 cm^{-1} range where the



rms for the extended case is on average 3% better than the baseline value with a 5% peak attained at 875 cm^{-1} . Between 1200 cm^{-1} and 1400 cm^{-1} the improvement is only marginal, the rms for the extended case being on average 0.05% better than the baseline value. Results for the bias are mixed.

As for the CAMEX-1 case, these results suggest that the use of this particular revised list of water parameters has a positive impact especially on rms scores. This stresses the importance of improved molecular parameters in reducing the total system noise. It should be noted, however, that these results are to some extent affected by the inconsistency between the formulation of the water continuum used in GENLN2 (based on the molecular parameters available in the HITRAN-96 database) and the revised molecular database used in the line-by-line calculations for the extended case. In principle, the parameterization of the water continuum should be reformulated based on the revised molecular database but this is far beyond the scope of this paper.

5.3 Sensitivity to changes in temperature and humidity profiles

An exercise similar to that described in section 3.4 was carried out for the ARM-WVIOP case as well. The dataset contains estimates of the water vapor and temperature uncertainties. A major difference to the CAMEX-1 case is that the uncertainty values are not an upper limit but random errors (1 standard deviation) derived from statistical variability of the various measurements during the averaging period. Radiosonde uncertainties were derived from the inter-batch variability observed in dual-sonde launches over the course of the IOP. The temperature and water vapor mixing ratio error profiles are shown in Figure 16. Errors in mixing ratio are typically between 10 and 20% in the 980 to 300 hPa range, while the error can be as great as 30% at lower pressures. For temperature, errors are less than 0.2%. As for the CAMEX-1 case, we computed GENLN2 spectra by increasing and decreasing the average temperature and water vapor profiles by the error profile. Results are shown in Fig. (a) for temperature and 17(b) for water vapor, where the relative bias for the perturbed case (defined in section 3.4) is plotted with the relative bias and the relative rms for the reference case. These results suggest that uncertainties in the characterization of the temperature profiles are likely not to have resulted in any significant impact on the accuracy of the calculations. As for the humidity profile, part of the bias in the 700 to 1400 cm^{-1} range could be explained in terms of uncertainties in the water vapor profile, but the large differences seen in Fig. 12 across the water vapor vibro-rotational band cannot be attributed to profiling uncertainties. Again, the close match between bias and rms (not shown) suggests than one of the effects of having perturbed the atmospheric profiles is to impart an offset to the radiances.

6. Conclusions

Two test cases are examined where simulated spectra are compared to spectra measured during the first Convection and Moisture Experiment (CAMEX-1) campaign and during a Water Vapor Intensive Observing Period at the Atmospheric Radiation Measurement (ARM) site. A special emphasis is given to the up-welling radiance spectra measured by the High-resolution Interferometer Sounder (HIS) instrument during the CAMEX-1 campaign, because of the similarity in viewing geometry with the next generation atmospheric sounders AIRS and IASI. The primary objective of the paper is to quantify differences due to different forward model mechanics and to the quality of the spectroscopic databases used in the forward model computations, and to identify spectral regions where forward model errors are smallest.



The simulations are performed using two very different LBL codes, HARTCODE and GENLN2, in very controlled conditions, with a pre-defined atmospheric layering and surface conditions.

The data measured during both cases is the result of averaging of individual spectra: during the CAMEX-1 case the signal is averaged over an atmospheric path of about 50 km, while in the ARM case 15 individual spectra are averaged, covering a period of about two hours. In both cases therefore the estimated measurement standard deviation incorporates the spectral variations induced by true atmospheric variability during the measuring period.

For the CAMEX-1 case the two LBL codes produce very similar results. In most spectral regions the difference between simulation and measurement is much larger than the difference between the two codes, which are highly correlated. This result suggests that most of the discrepancies with measurements are not due to the particular code mechanics but to insufficient knowledge in basic spectroscopy. Similar conclusions are reached for the ARM case, but the differences between the results of the two codes are larger than in the CAMEX-1 case. When the root mean square difference between simulation and measurement is expressed in terms of NEDT at 280 K, we note that the values are larger than the value of 0.2-0.4 K which is usually adopted when simulating the forward model error in studies of the total error budget for atmospheric sounders. In HIS band 1 values range from 0.25 to 1.5 K until 1000 cm^{-1} , while in band 2 the NEDT ranges from 0.25 to 0.6 K. For the ARM case the NEDT differences are much higher, ranging from 0.5 to 2.4 K from 600 to 1400 cm^{-1} , and up to 5.5K in the water vapor band centered at 16 microns.

Spectra at higher sampling have been used to investigate the spectral structure of the differences between simulations and measurements. Results show that in the important temperature sounding region 730 - 770 cm^{-1} the CO_2 line has a fairly regular spacing and the largest (negative) deviations are very close, but not coincident, with line centers; between the main lines however systematically positive deviations are observed with a magnitude about half the maximum (negative) local “errors”. In presence of isolated water vapor lines these positive deviations are of larger magnitude. In the window region the deviations are largest in presence of single or a small group of water vapor lines. The largest differences are in general seen in correspondence with groups of tightly spaced lines, a far from uncommon situation since one cannot speak of wings between lines in most part of the range under consideration. These results indicate however that it is possible to identify spectral regions, that have been pointed out and discussed in the previous sections, where the simulations are closer to the measurements.

During the course of this study a revised list of water parameters became available and was used to test the impact of improved spectroscopic data on the accuracy of the line-by-line calculations. The results suggest that the use of the revised parameters can have a positive impact on the bias and rms scores. In particular it has resulted in a rms that is lower, sometimes significantly lower, than the baseline value throughout most of the considered spectral range. Improved water vapor spectroscopic parameters are clearly needed, as documented especially by the results of the ARM case, across the whole vibro-rotational band of water vapor.

The assessment of the accuracy that can be achieved by the forward model calculations in absolute terms, require an improved treatment of the surface parameters with respect to the baseline values that were selected for the CAMEX-1 comparison. This was achieved using a spectrally varying emissivity formulation, together with computation of the downwelling radiance at the surface and a change to the skin temperature used for the computations. The overall effect of having revised the surface parameters has been to significantly improve the absolute accuracy of the line-by-line computations in the 11 micron window region.



Although a detailed assessment of the errors resulting from uncertainties in the temperature and humidity profiles is outside the scope of the present paper, the “extreme” relative humidity values contained in the CAMEX-1 dataset, and the standard deviation estimates in the ARM dataset, were used to investigate the sensitivity to changes in humidity. For the CAMEX-1 case, the difference between the simulations in HIS band 2 is well above the differences with measurements, at least in the spectral regions whose weighting functions peak in the mid to upper troposphere. In the ARM case part of the bias in the 700 to 1400 cm^{-1} range can be explained in terms of uncertainties in the water vapor profile, but no sensitivity is seen across the vibro-rotational band of water vapor. In the ARM case an estimate of temperature error is also provided. The results suggest that uncertainties in the characterization the temperature profiles are likely not to have resulted in any sensible impact on the accuracy of the calculations. The close match between bias and rms suggests that one of the effects of having perturbed the atmospheric profiles is to impart an offset to the radiances.

Acknowledgements

The comparison was made possible by the dedicated work of R. Knuteson, P. Van Delst and D. Tobin, CIMSS, that provided the data sets and the information required to adequately process the simulated data. L. Strow, University of Maryland, provided the revised list of water line parameters prepared by R.A. Toth, JPL. N. Husson, LMD, created an update of the GEISA database with the new data. M. Matricardi is supported by EUMETSAT (contract EUM/CO/98/678/DD through the IASI pre-launch definition studies. R. Rizzi is supported by EUMETSAT (contract EUM/CO/96/390/DD) and by ASI (Agenzia Spaziale Italiana).

References

1. J.R. Eyre, G.A. Kelly, A.P. McNally, E. Anderson and A. Persson, 1993: Assimilation of TOVS radiance information through one-dimensional variational analysis. *Q.J.Roy. Meteor. Soc.*, **119**, 1427-1463.
2. F. Rabier, J. Thépaut and P. Courtier, 1998: Extended assimilation and forecast experiments with a four dimensional variational assimilation system. *Q.J.Roy. Meteor. Soc.*, **124**, 1861-1887.
3. M. Matricardi and R. Saunders, 1999: Fast radiative transfer model for simulation of infrared atmospheric sounding interferometer radiances. *Appl. Opt.*, **38**, 5679-5691.
4. <http://www-projet.cst.cnes.fr:8060/IASI/index.html>
5. <http://www-air.jpl.nasa.gov/>
6. V.L. Griffin, A.R. Guillory, M. Susko and J.E. Arnold, 1994: Operations Summary for the Convection and Moisture Experiment (CAMEX-1), NASA Technical memorandum, NASA TM-108445.
7. Stokes GM and SE Schwartz, 1994: The Atmospheric Radiation Measurement (ARM) Program: programmatic background and design of the cloud and radiation test bed. *Bull. Am. Meteor. Soc.*, **75**, 1201-1221.
8. W.L. Smith, H. E. Revercomb, H.B. Howell, and H.M. Wolf, 1983: HIS- A satellite instrument to observe temperature and moisture profiles with high resolution. In *Fifth Conference on Atmospheric Radiation*, American Meteorological Society, Boston.
9. D.P. Edwards, 1992: GENLN2. A general Line-by-Line Atmospheric Transmittance and Radiance Model, NCAR Technical note NCAR/TN-367+STR, National Center for Atmospheric Research, Boulder,Co.



10. B.H. Armstrong: 1967: Spectrum line profiles: the Voigt function. *J. Quant. Spectrosc. Radiat. Transfer*, **7**, 66-88.
11. Cousin, C., R. le Doucen, C. Boulet and H. Henry, 1985: Temperature dependence of the absorption in the region beyond the 4.3 μm band head of CO_2 . Part 2: N_2 and O_2 broadening, *Applied Optics* **24**, 3899-3907.
12. L.L. Strow, D.C. Tobin and S.E. Hannon, 1994: A compilation of First-Order Line-Mixing coefficients for CO_2 Q-branches. *J. Quant. Spectrosc. Radiat. Transfer*, **52**, 281.
13. S.A. Clough, F.X. Kneizys, R. Davies, R. Gamache and R. Tipping, 1980: Theoretical line shape for H_2O vapour; Application to the continuum. In *Atmospheric water vapour*, A. Deepak, T.D. Wilkerson and L.H. Ruhnke, eds. (Academic Press, New York), pp. 25-46.
14. S.A. Clough, F.X. Kneizys and R.W. Davis, 1989: Line shape and the water vapour continuum. *Atmospheric Research*, **23**, 229-241.
15. V. Menoux, R. Le Doucen, C. Boulet, A. Roblin and A.M. Bouchardy, 1993: Collision induced absorption in the fundamental Band of N_2 . *Applied Optics*, **32**, 263-268.
16. Y.M. Timofeyev and M.V. Tonkov, 1978: Effect of the induced Oxygen absorption band on the transformation of radiation in the 6 μm region of the Earth's atmosphere. *Atmos. Ocean Phys.*, **14**, 437-441.
17. C.P. Rinsland, J.S. Zander, J.S. Namkung, C.B. Farmer and R.H. Norton, 1989: Stratospheric infrared continuum absorption observed by the ATMOS instrument. *J. Geophys. Res.*, **94**, 16303-16322.
18. F. Miskolczi, R. Rizzi, R. Guzzi, M. Bonzagni, 1989: A new high resolution transmittance code and its application in the field of remote sensing. In: *IRS'88: Current Problems in Atmospheric Radiation*, A. Deepak Publishing, pp. 388-391.
19. F. Miskolczi, M. Bonzagni, R. Guzzi, 1990: High Resolution Atmospheric Radiance-Transmittance Code (HARTCODE). *Meteorology and Environmental Sciences*, World Scientific Pub. Co., pp. 743-790.
20. Rodriguez R, KW Jukus, N Lacombe, G Blanquest, J Valrand, WA Traub, B Khalil, R LeDoucent, A Valentin, C Camy-Peiret, L Bonamy and JM Hartmann, 1999: Model, software and data base for computation of line mixing effects in infrared Q branches of atmospheric CO_2 . I. Symmetric isotopomers. *J. Quant. Spectrosc. Radiat. Transfer*, **61**, 153-184.
21. FASCOD 3, 1989: Spectral simulation. Proceedings of the International Radiation Symposium. IRS'88 Eds. J. Lenoble and J.F. Geleyn. Deepak Publishing Co.
22. Robert Knuteson, CIMSS, personal communication.
23. H.F. Revercomb, F.A. Best, R.G. Dedecker, R.P. Dirks, A. Herbsleb, R.O. Knuteson, J.F. Short, and W.L. Smith, 1993: Atmospheric Emitted Radiance Interferometer (AERI) for ARM. In *Fourth Symposium on Global Change Studies*, Anaheim, CA, January 17-22 1993, Published by the American Meteorological Society, Boston, Mass.
24. http://www.arm.gov/docs/iops/1997/sep_integrated/index.html
25. N. Jaquinet-Husson, E. Arié, J. Ballard, A. Barbe, G. Bjoraker, B. Bonnet, L.R. Brown, C. Camy-Peyret, J.P. Champion, A. Chedin, A. Chursin, C. Clerbaux, G. Duxbury, J.-M. Flaud, N. Fourrié, A. Fayt, G. Graner, R. Gamache, A. Goldman, V.I. Golovko, G. Guelachvili, J.M. Hartmann, J.C. Hilico, J. Hillman, G.



- Lefèvre, E. Lellouch, S.N. Mikhailenko, O.V. Naumenko, V. Nemtchinov, D.A. Newnham, A. Nikitin, J. Orphal, A. Perrin, D.C. Reuter, C.P. Rinsald, L. Rosenmann, L.S. Rothman, N.A. Scott, J. Selby, L.N. Sinitsa, J.M. Sirota, A.M. Smith, K.M. Smith, Vl. G. Tyuterev, R.H. Tipping, S. Urban, P. Varanasi and M. Weber, 1999: The 1997 spectroscopic GEISA databank. *J. Quant. Spectrosc. Radiat. Transfer*, **62**, 205-254.
26. L.S. Rothman, C.P. Rinsland, A. Goldman, S.T. Massie, D.P. Edwards, J.-M. Flaud, A. Perrin, C. Camy-Peyret, V. Dana, J.-Y. mandin, J. Schroeder, A. McCann, R.R. Gamache, R.B. Watson, K. Yoshino, K.V. Chance, K. W. Jucks, L.R. Brown, V. Nemtchinov, and P. Varanasi, 1998: The HITRAN molecular spectroscopic database and HAWKS (HITRAN Atmospheric Workstation): 1996 edition. *J. Quant. Spectrosc. Radiat. Transfer*, **60**, 665-710.
27. L.S. Rothman, R.R. Gamache, R.H. Tipping, C.P. Rinsald, M.A.H. Smith, D. Chris Benner, V. Malathy Devi, J.-M. Flaud, C. Camy-Peyret, A. Perrin, A. Goldman, S.T. Massie, L.R. Brown and R.A. Toth, 1992: The HITRAN molecular database: editions of 1991 and 1992. *J. Quant. Spectrosc. Radiat. Transfer*, **48**, 469-507.
28. R. A. Toth, 1998: Water vapour measurements between 590 and 2582 cm^{-1} : Line Positions and Strenghts. *J. Molecular Spectroscopy*, **190**, 379-396.
29. R.A. Toth, L.R. Brown and C. Plymate, 1998: Self-broadned widhts and frequency shifts of water vapour lines between 590 and 2400 cm^{-1} . *J. Quant. Spectr. R. T.*, **59**, 529-652.
30. R.A. Toth, 1999: Analysis of Line Positions and Strenghts of H_2^{16}O Ground and Hot bands Connecting to Interacting Upper States: (020), (100), and (001). *J. Molecular Spectroscopy*, **194**, No.1, 28-42.
31. R.A. Toth, 1999: HDO and D_2O Low Pressure, Long Path Spectra in the 600-3100 cm^{-1} Region HDO Line positions and Strenght. *J. Molecular Spectroscopy*, **195**, 73-97.
32. R.A. Toth, 1999: Air-and N_2 -Broadening Parameters of HDO and D_2O , 709 to 1936 cm^{-1} . *J. Molecular Spectroscopy*, **198**, 358-360.
33. R.A. Toth, 2000: Air- and N_2 -Broadening Parameters of Water vapor: 604 to 2271 cm^{-1} . *J. Molecular Spectroscopy*, **201**, No.2, 218-243.
34. Nicole Husson, LMD, personal communication.
35. K. Masuda, T. Takashima and T. Takayama, 1988: Emissivity of pure sea waters for the model of sea surface in the infrared window regions. *Remote Sens. Environ.*, **24**, 313-329.
36. G.M. Hale and M.R. Querry, 1973: Optical constants of water in the 200-nm to 200- μm wavelenght region. *Appl. Opt.* **12**, 555-563.
37. D. Friedman, 1969: Infrared characteristics of ocean water (1.5-15 μm). *Appl. Opt.*, **8**, 2073-2078.

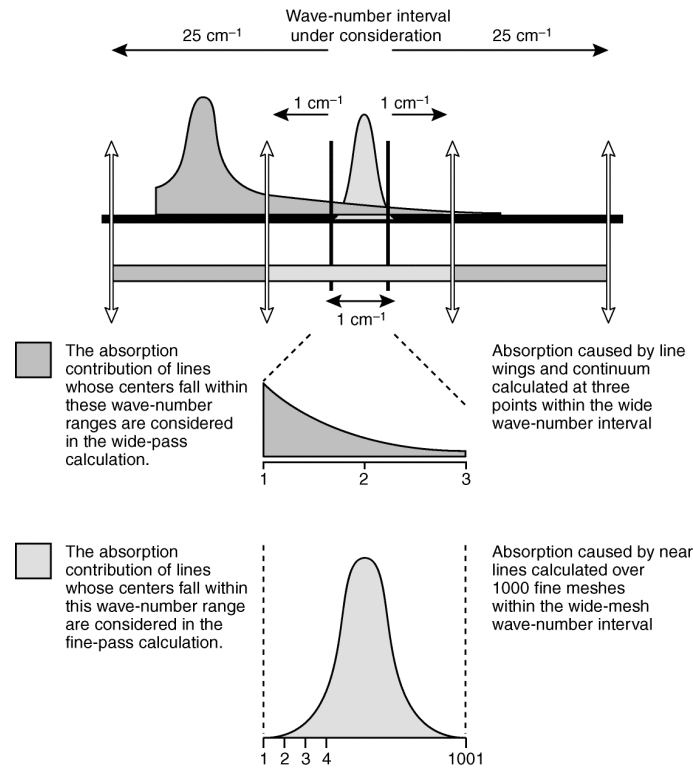


Fig 1 The spectral calculation scheme for HARTCODE.

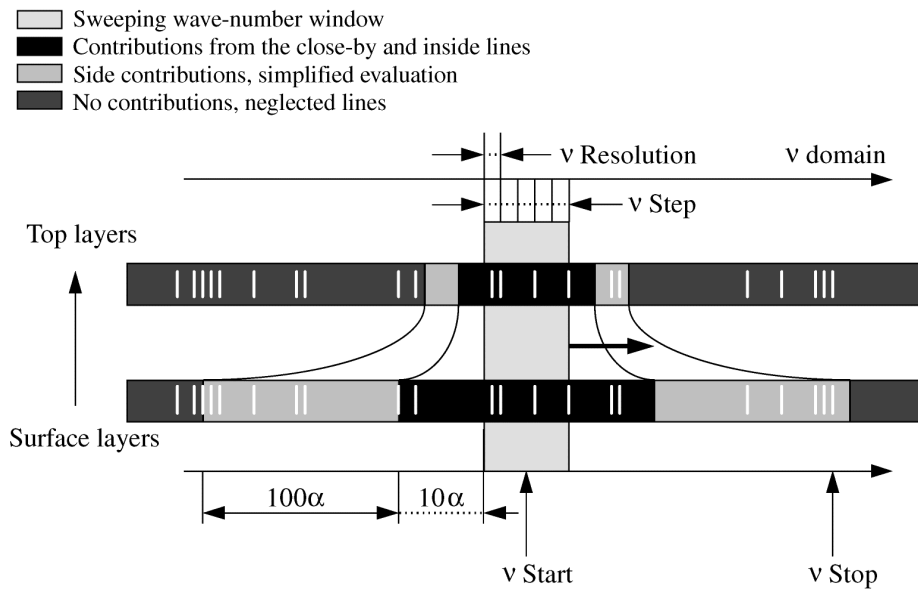


Fig 2 The spectral calculation scheme for GENLN2.

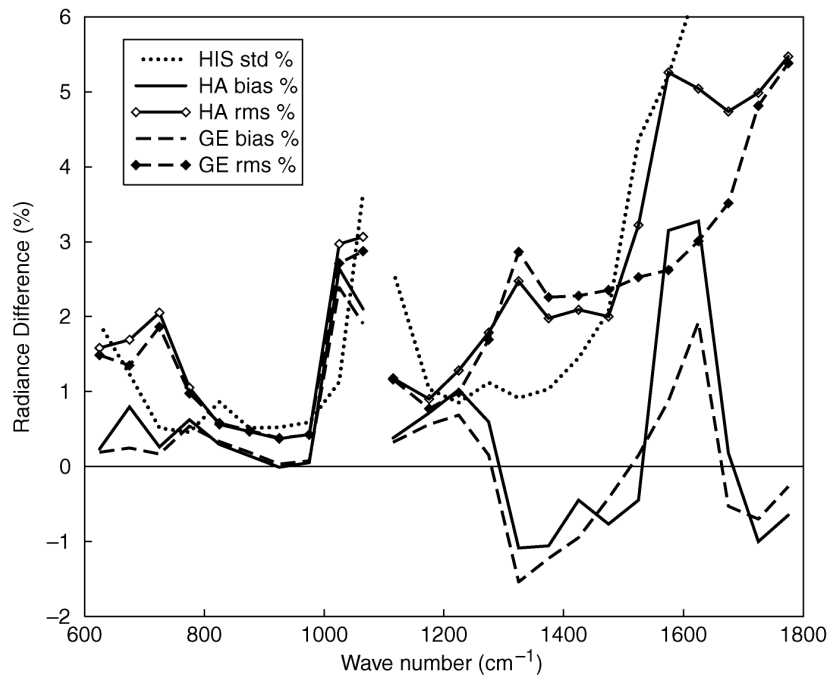


Fig 3 Relative bias and root-mean-square-error of the difference between simulated (HARTCODE, HA, and GENLN2, GE) and measured spectra for the CAMEX-1 case. Values for HIS band-1 and band-2 are computed over intervals of 50 cm^{-1} width. The relative standard deviation of the HIS measurement is also shown (dotted line).

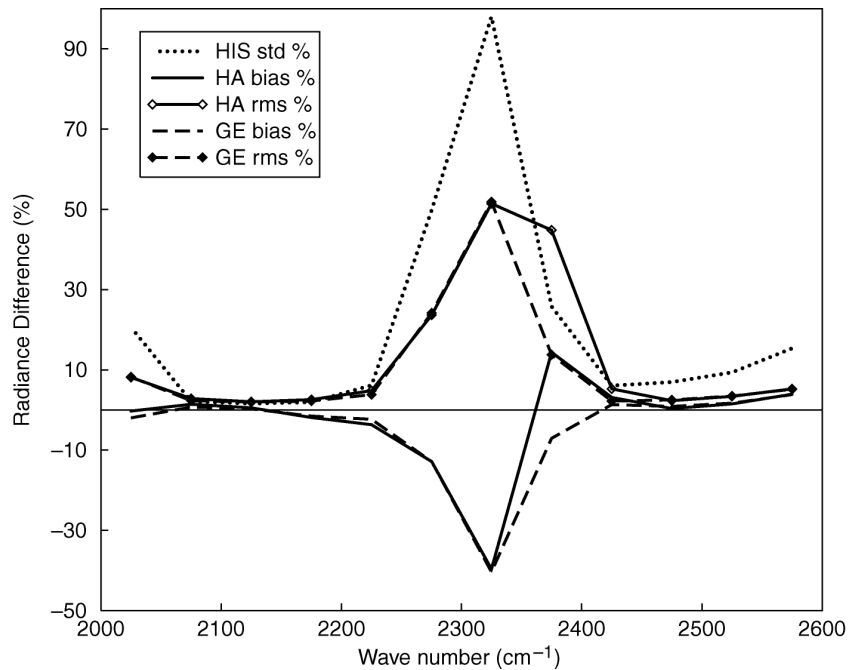


Fig 4 Same as Fig. 3 for HIS band 3.

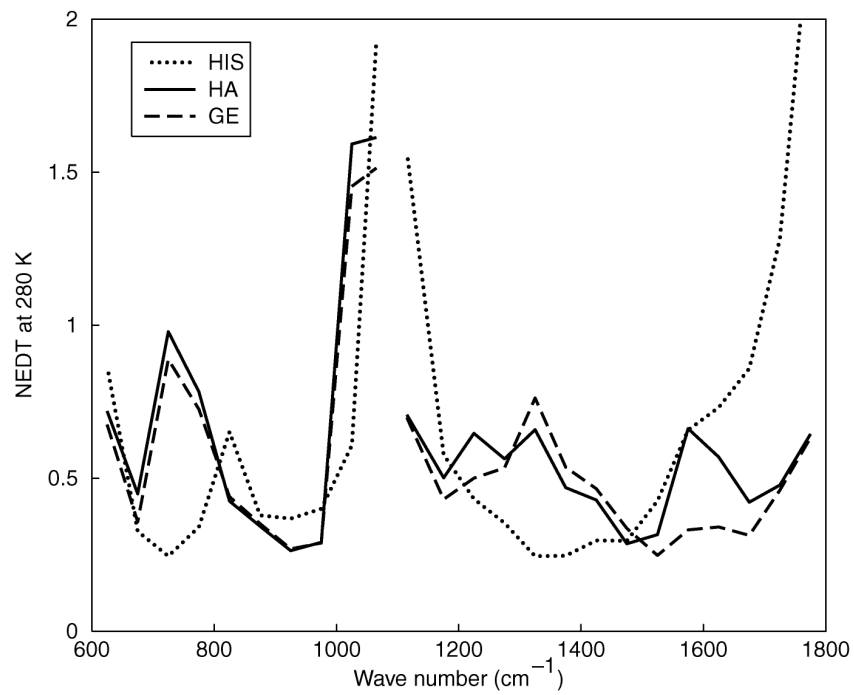


Fig 5 Root-mean-square-error of the difference between simulated (HARTCODE, HA, and GENLN2, GE) and measured spectra, over intervals of 50 cm^{-1} width, expressed as NEDT for a blackbody temperature of 280K. The estimated HIS measurement error is also shown (HIS) as a dotted curve.

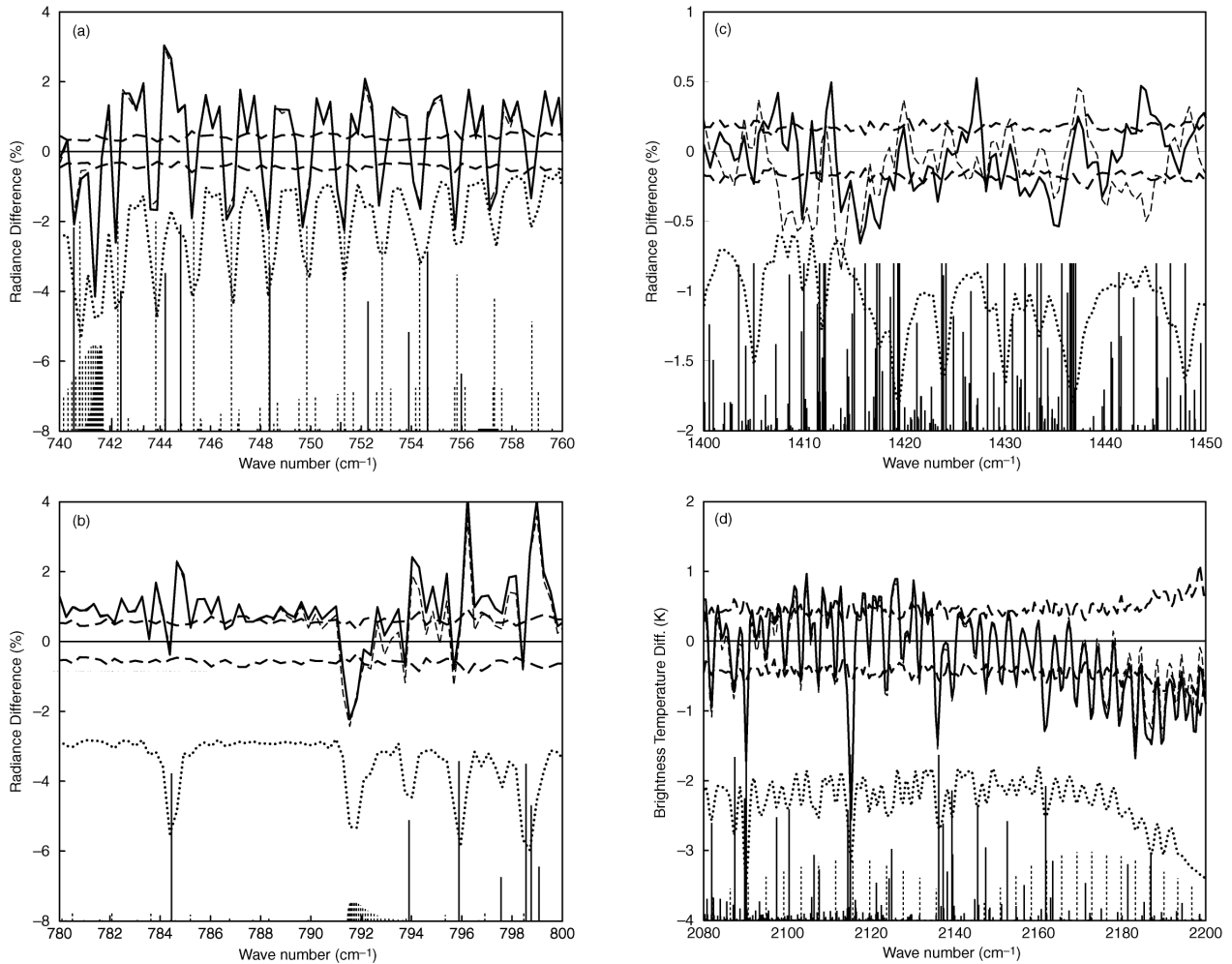


Fig 6 Examples showing the correlation between GENLN2 (GE) and HARTCODE (HA) spectra for the CAMEX-1 case. The lower dotted curve is the HIS radiance spectrum (the ordinate scale is not relevant). The upper solid curve is the HARTCODE spectrum minus the HIS spectrum. The upper dotted curve is the GENLN2 spectrum minus the HIS spectrum and the two dashed curves identify the positive and negative HIS estimated measurement error (std). Absorption lines from H₂O and CO₂ are also shown as lower solid and lower dotted vertical lines respectively. Data are shown in four spectral intervals: (a) 740-760 cm⁻¹; (b) 780-800 cm⁻¹; (c) 1400-1450 cm⁻¹; (d) 2080-2200 cm⁻¹.

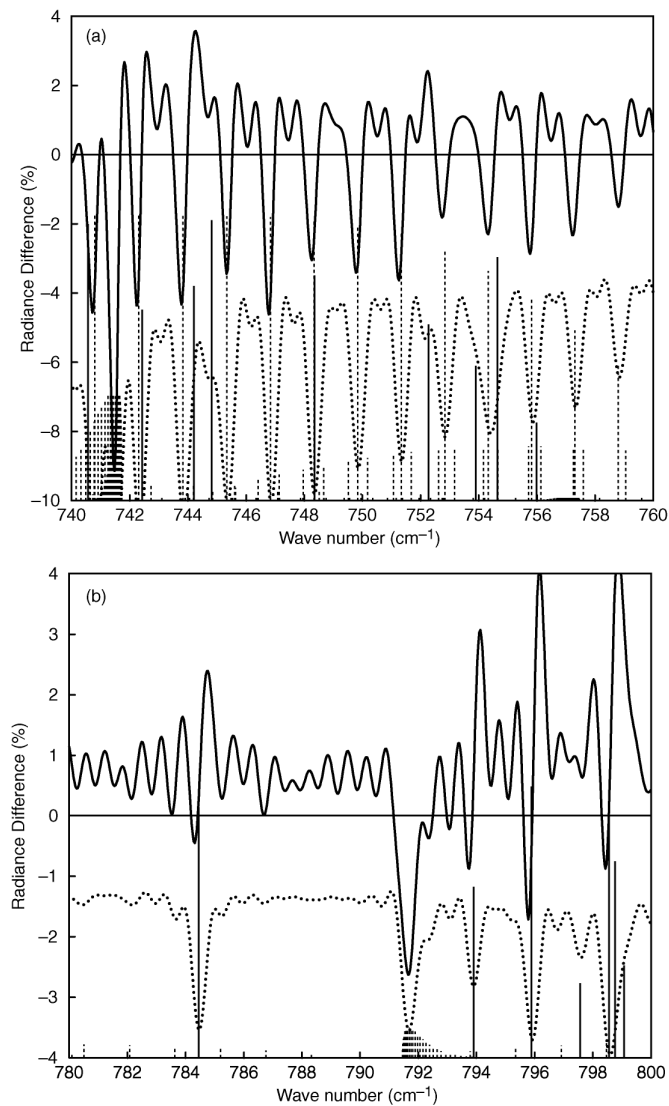


Fig 7 Spectra obtained by re-sampling the HIS and HARTCODE spectra for the CAMEX-1 case. The upper solid curve is the difference between HARTCODE simulations and measurements at higher spacing and the lower dotted curve is the measured spectrum at higher sampling. Absorption lines from H₂O and CO₂ are also shown as lower solid and lower dashed vertical lines respectively. Data are shown in two spectral intervals: (a) 740-760 cm⁻¹; (b) 780-800 cm⁻¹.

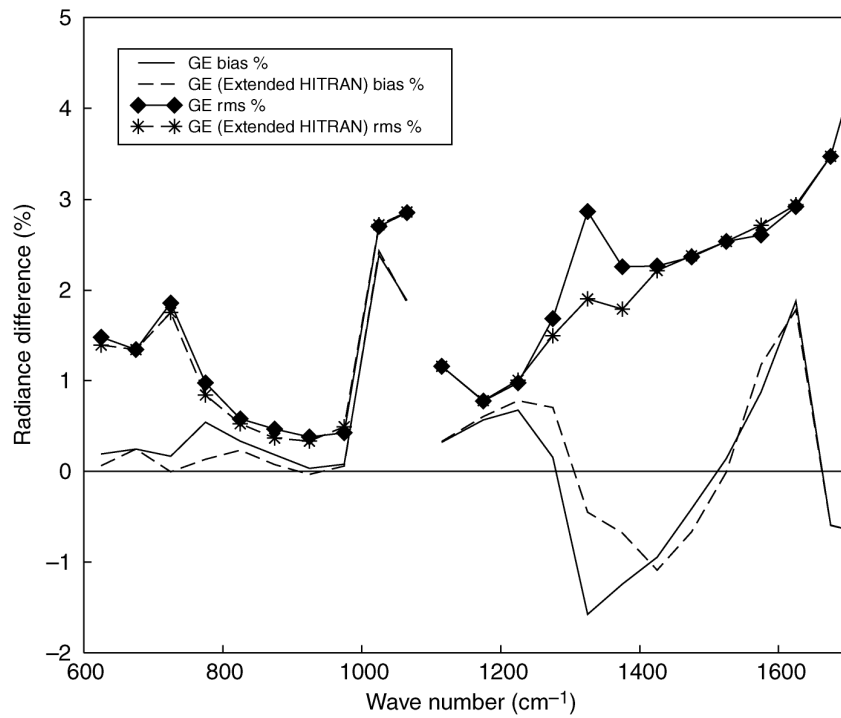


Fig 8 The relative bias and root-mean-square-error of the difference between GENLN2 and measured spectra for the CAMEX-1 case. The Spectrum computed using the extended HITRAN-96 database (GE (Extended HITRAN)) is compared with that computed using the reference HITRAN-96 (GE). Values are computed over intervals of 50 cm⁻¹ width.

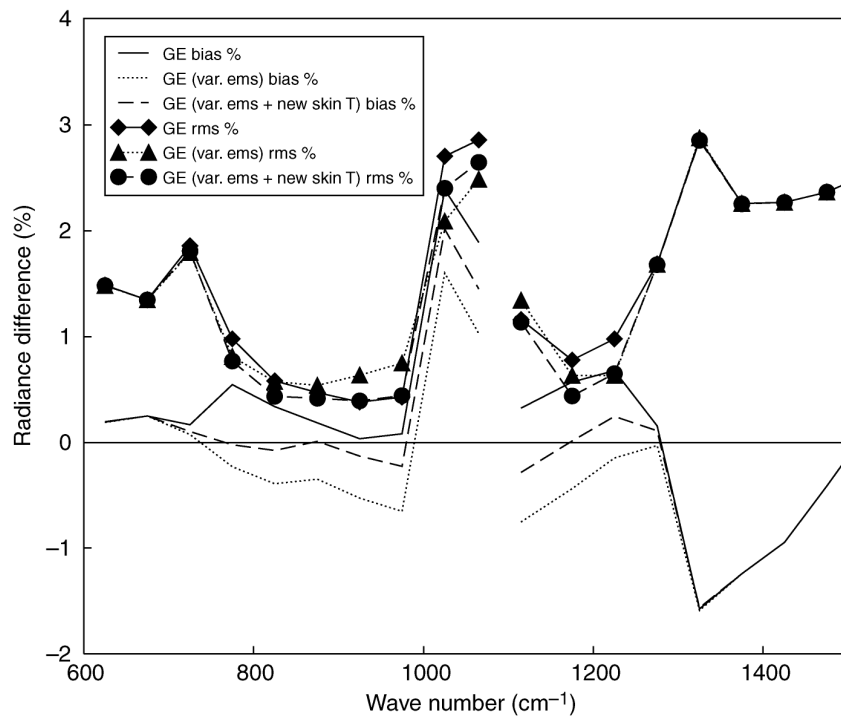


Fig 9 The relative bias and root-mean-square-error of the difference between GENLN2 and measured spectra for the CAMEX-1 case. Spectra computed using a variable emissivity (GE (var. ems)) and a variable emissivity plus a revised skin temperature (GE (var. ems + new skin)) are compared with those computed using the emissivity and skin temperature reference values (GE).

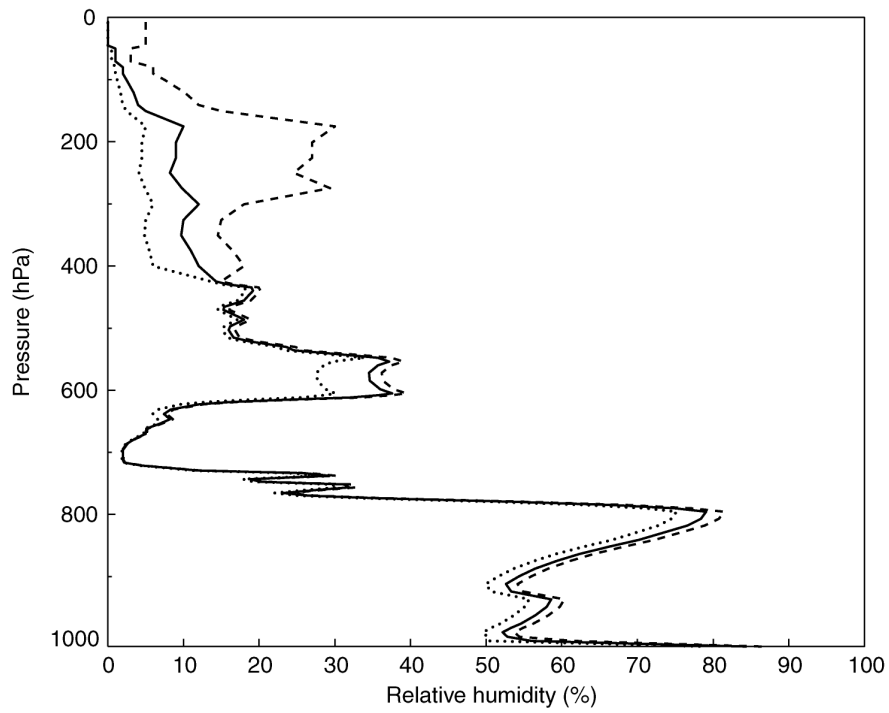


Fig 10 The relative humidity error profile for the CAMEX-1 case.

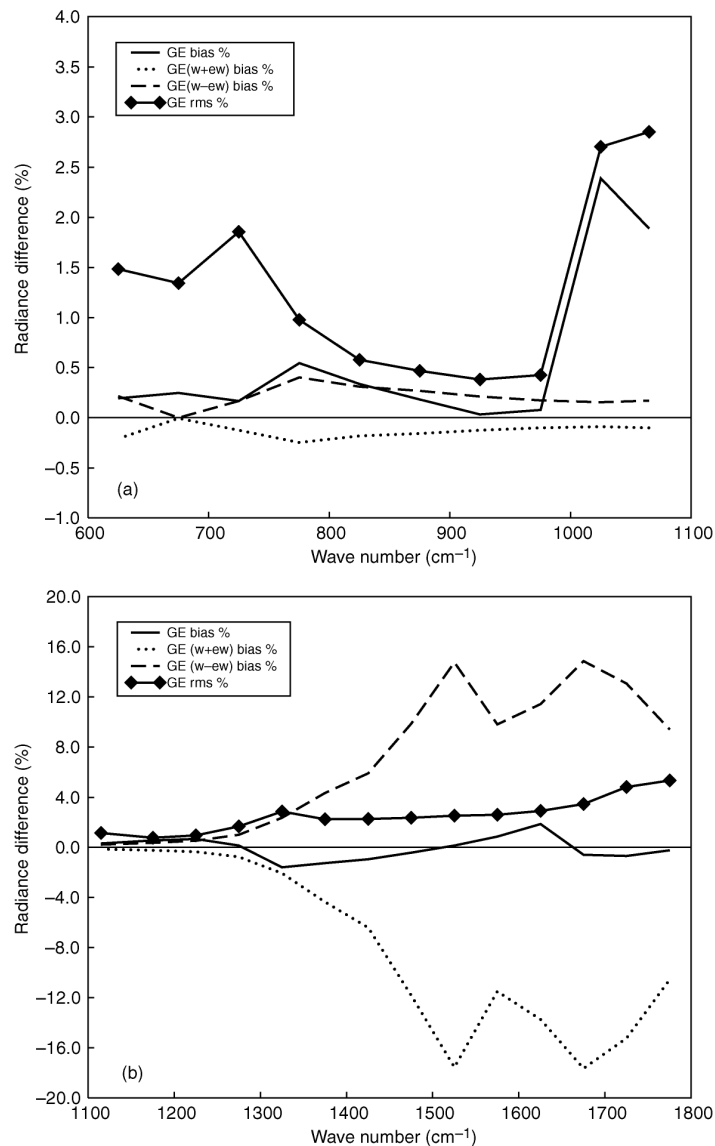


Fig 11 The relative bias of the difference between the reference GENLN2 spectra and those computed by increasing (GE (w+ew)) and decreasing (GE (w-ew)) the water vapour profile by the error profile for the CAMEX-1 case. The relative bias and root-mean-square-error of the difference between the reference GENLN2 spectra and the measured spectra is also shown as solid and solid-diamond line (GE). Values computed over intervals of 50 cm⁻¹ width are shown for: (a) band-1; (b) band-2.

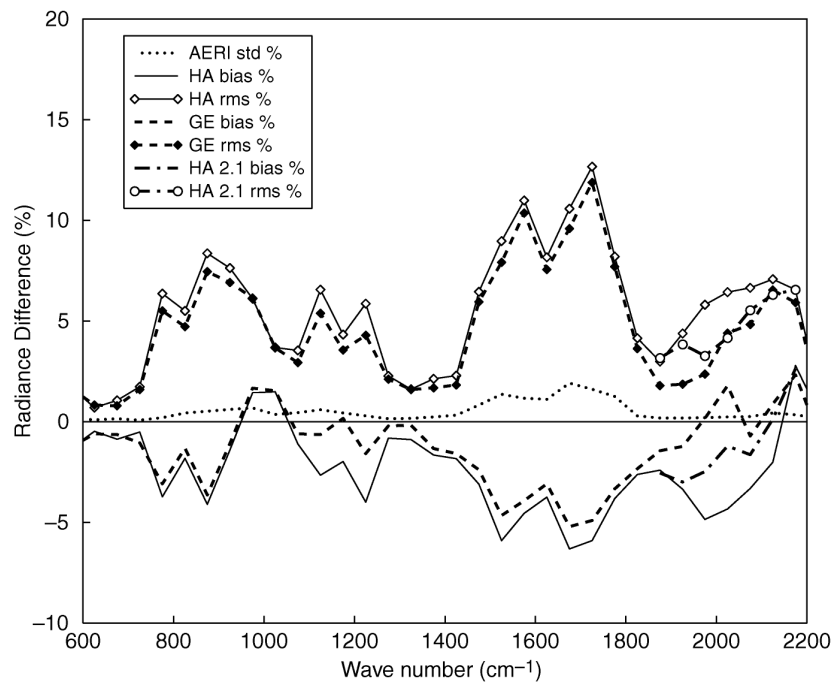


Fig 12 Relative bias and root-mean-square-error of the difference between simulated (HARTCODE, HA, and GENLN2, GE) and measured spectra for the ARM-WVIOP case. Values are computed over intervals of 50 cm-1 width. The estimated AERI measurement error is also shown as a dotted curve.

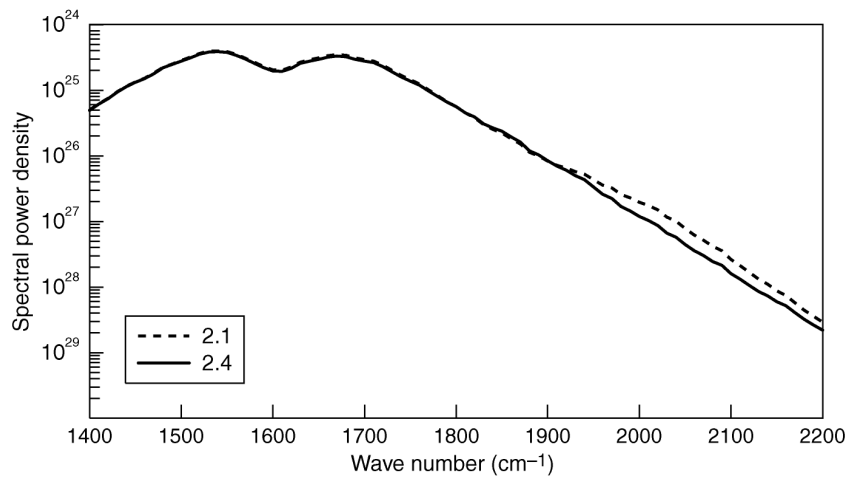


Fig 13 . Spectral power density for the water vapor CKD foreign broadening coefficients- The solid line is version 2.4 used by HARTCODE and the dotted line are the version 2.1 used by GENLN2.

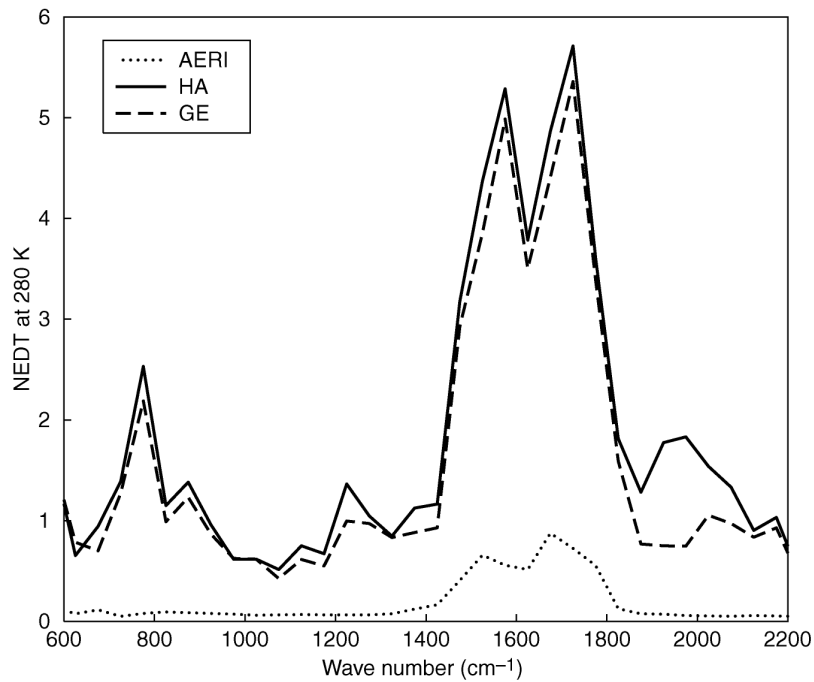


Fig 14 Root-mean-square-error of the difference between simulated (HARTCODE, HA, and GENLN2, GE) and measured spectra, over intervals of 50 cm-1 width, expressed as NEDT for a blackbody temperature of 280K. The estimated AERI measurement error is also shown as a dotted curve.

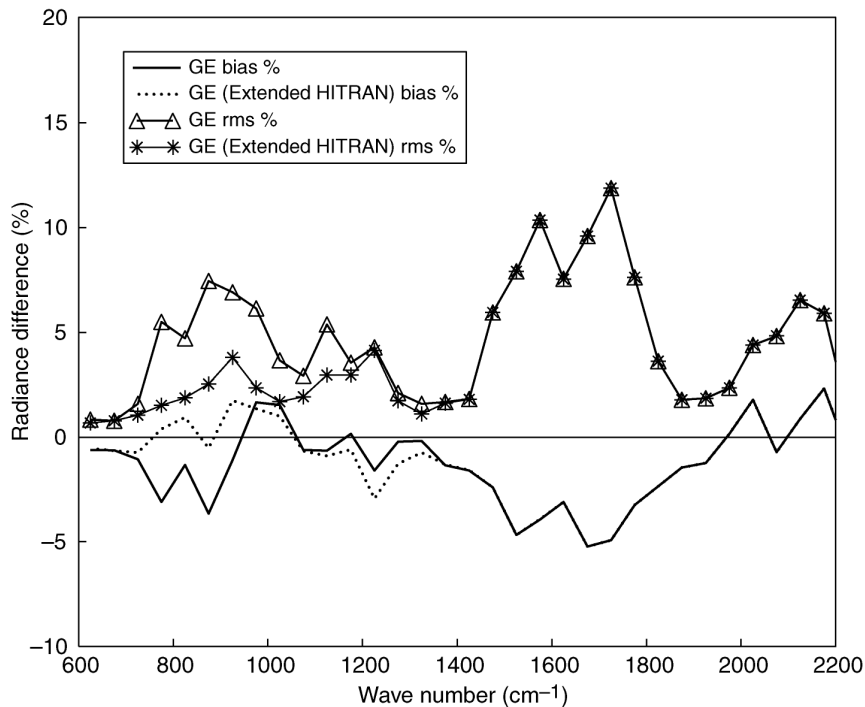


Fig 15 The relative bias and root-mean-square-error of the difference between GENLN2 and measured spectra for the ARM-WVIOP case. The spectrum computed using the extended HITRAN-96 database (GE (Extended HITRAN)) is compared with that computed using the reference HITRAN 96 (GE). Values are computed over intervals of 50 cm-1.

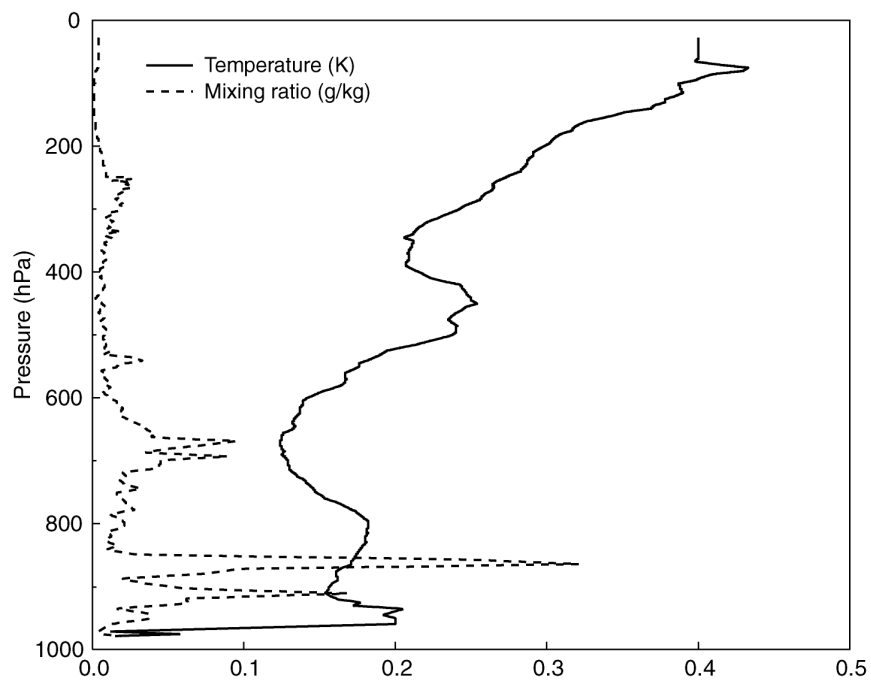


Fig 16 The ARM-WVIOP case error profile for temperature and water vapour mixing ratio.

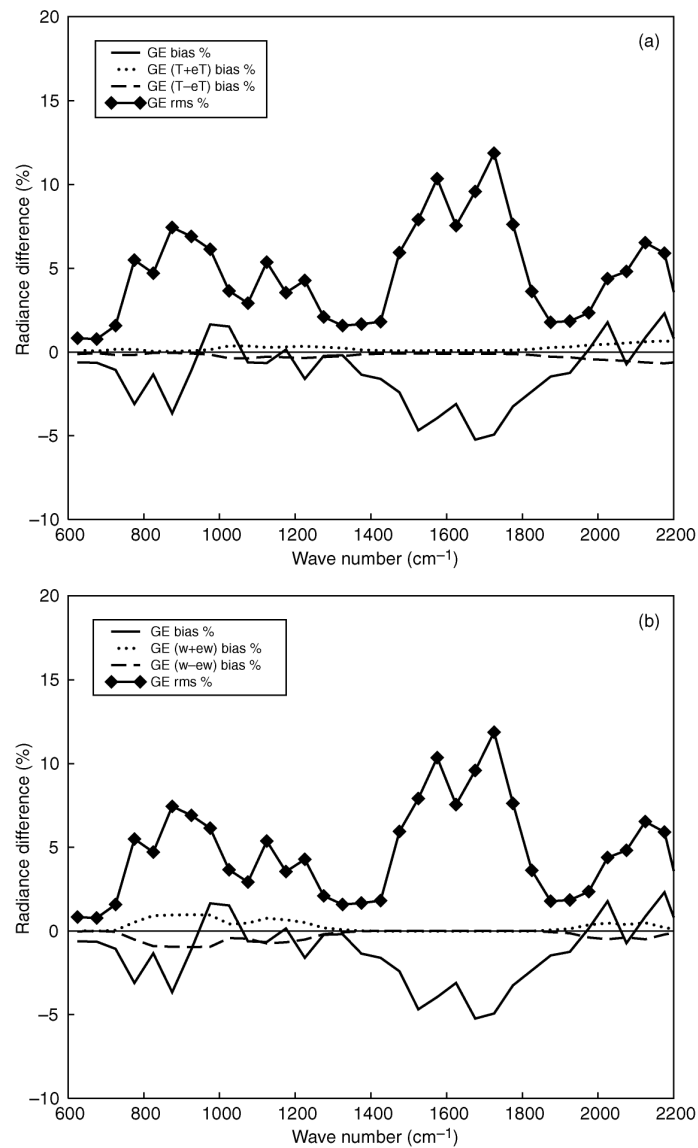


Fig 17 The relative bias of the difference between the reference GENLN2 spectra and those computed by: (a) increasing ($GE(T+eT)$) and decreasing ($GE(T-eT)$) the temperature profile by the error profile; (b) increasing ($GE(w+ew)$) and decreasing ($GE(w-ew)$) the water vapor profile by the error profile, are shown for the ARM-WVIOP case. The relative bias and root-mean-square-error of the difference between the reference GENLN2 spectra and the measured spectra is also shown as solid and solid-diamond line (GE). Values are computed over intervals of 50 cm^{-1} width.